JOURNAL OF AIRCRAFT
Vol. 40, No. 4, July–August 2003

Stability Analysis of a Tethered Aerostat

Casey Lambert* and Meyer Nahon†
McGill University, Montreal, Quebec H3A 2K6, Canada

This paper presents a dynamics analysis of a streamlined aerostat tethered to the ground by a single tether. A nonlinear dynamics model of this system is first assembled. The tether is modeled using a lumped mass approach, and the viscoelastic properties of the tether are included. The aerostat is modeled using a component breakdown approach. The dynamics equations of the cable and aerostat are then assembled into a single system of nonlinear differential equations. A linearization of this system is then performed using a finite difference approach. The resulting linear equations of motions are decoupled into longitudinal and lateral subsets. The stability properties of each subset is then studied as a function of wind speed. The effect of varying tether length is also investigated.

Nomenclature

A	=	hull cross-sectional area or fin aspect ratio
$\boldsymbol{A}, \boldsymbol{A}_{\text{lat}}, \boldsymbol{A}_{\text{long}}$	=	state matrices for complete system, lateral and longitudinal subsystems
A_f	=	fin planform area
A_h	=	cross-sectional area of hull at $\xi = l_h$
A_t	=	tether cross-sectional area
$\boldsymbol{a}_B$	=	aerostat mass-center acceleration
b, b_c	=	tether damping coefficient and critical damping coefficient
$(Cd_h)_0, (Cd_c)_h$	=	hull zero-angle axial and crossflow drag coefficients
C_D, C_{D0}	=	fin drag coefficient, fin parasitic drag coefficient
C_d	=	normal drag coefficient of cable element
C_L	=	fin lift coefficient
$C_{l\alpha}, C_{L\alpha}$	=	slope of the two-dimensional lift curve, slope of the three-dimensional lift curve
D, D_H, D_t	=	drag force, hull drag force, tether drag force
d_t	=	tether diameter
E	=	Young's modulus of the cable
e	=	Oswald's efficiency factor
$\boldsymbol{F}_B$	=	net force applied to aerostat
$\boldsymbol{F}_b$	=	buoyancy force
$\boldsymbol{F}_i$	=	force from the body component i ($i = H, P, S, U$ representing the hull, port fin, starboard fin, and upper fin, respectively)
$\boldsymbol{F}_t$	=	force from the tether
g	=	gravitational acceleration
$\boldsymbol{I}$	=	inertia tensor for aerostat
I_1, I_3, J_1, J_2	=	hull-related geometric quantities
k_1, k_3	=	axial and lateral added-mass coefficients for hull
L, L_H, L_t	=	lift force, hull lift force, tether length
l_h	=	distance from aerostat nose to starting point of tailfins
l_i, l_i^u	=	stretched and unstretched length cable element i
$\boldsymbol{M}_i$	=	moment caused by the body component i ($i = H, P, S, U$)
M_{nose}	=	moment about the nose acting on hull
$\boldsymbol{M}_t$	=	moment from the tether
m, m_a, m_e	=	true mass, added mass, and effective mass of aerostat
$\boldsymbol{p}_i = [x_i\ y_i\ z_i]^T$	=	position of cable node i
q_0	=	steady-state dynamic pressure ($= \rho U_H^2/2$)
r	=	hull radius
$\boldsymbol{r}_i$	=	position vector from mass center to body component ($i = H, P, S, U$)
$\boldsymbol{r}_t$	=	position vector from mass center to tether attachment point
S_H	=	hull reference area, ($=$ (hull volume)$^{2/3}$)
T_i	=	tension in cable element i
$\boldsymbol{U}_i = [u_i\ v_i\ w_i]^T$	=	velocity of body component i ($i = H, P, S, U$) with respect to surrounding air
$\boldsymbol{u}_i$	=	velocity of geometric center of cable element i with respect to surrounding air
V	=	hull volume
$\boldsymbol{V}_B = [u\ v\ w]^T$	=	velocity of the aerostat mass center with respect to ground
$\boldsymbol{V}_i$	=	velocity of body component i ($i = H, P, S, U$) with respect to ground
$\boldsymbol{W}$	=	wind velocity
$\boldsymbol{X}, \boldsymbol{X}_{\text{lat}}, \boldsymbol{X}_{\text{long}}$	=	state vector for complete system, lateral and longitudinal subsystems
x_n	=	axial distance from nose to the hull center of pressure
α, β	=	angle of attack and sideslip angle
γ	=	angle of hull lift force in the y-z plane
ε	=	cable strain
ζ	=	damping ratio
η_k	=	hull efficiency factor
θ_0	=	zero wind pitch angle of aerostat
ξ	=	axial distance along hull from the nose
ρ, ρ_t	=	density of air; density of tether
τ_n	=	period of oscillatory modes
ψ, θ, ϕ	=	yaw, pitch, and roll angles
$\omega = [pqr]^T$	=	angular velocity of aerostat
ω_n, ω_d	=	natural frequency and damped natural frequency of oscillatory modes

Received 31 January 2002; revision received 28 January 2003; accepted for publication 15 March 2003. Copyright © 2003 by Casey Lambert and Meyer Nahon. Published by the American Institute of Aeronautics and Astronautics, Inc., with permission. Copies of this paper may be made for personal or internal use, on condition that the copier pay the $10.00 per-copy fee to the Copyright Clearance Center, Inc., 222 Rosewood Drive, Danvers, MA 01923; include the code 0021-8669/03 $10.00 in correspondence with the CCC.

*Doctoral Candidate, Department of Mechanical Engineering, 817 Sherbrooke St. W. Student Member AIAA.

†Associate Professor, Department of Mechanical Engineering, 817 Sherbrooke St. W. Senior Member AIAA.

I. Introduction

TETHERED aerostats are known to be useful in applications where a payload must be deployed at altitude for long durations. In these applications the energy consumed (and the resulting refueling requirement) by a powered heavier-than-air craft renders that platform less competitive in relation to an aerostat that consumes no energy. However, tethered aerostats can be difficult to deploy and operate because of their large size, sensitivity to environmental conditions, and particular dynamics characteristics.

A group of radio astronomers at the National Research Council in Canada is interested in using a tethered aerostat system to support

the receiver of a large-scale radio telescope.[1] As part of the proof-of-concept experiment for this system, they are presently deploying a tethered aerostat in Penticton, British Columbia, to study its performance in this application. A parallel analytical/computational study is being conducted to study this system's dynamic characteristics.

Previous dynamics investigations of tethered aerostats can be separated into nonlinear and linear studies. DeLaurier[2] was first to study the nonlinear dynamics of an aerostat attached to a comprehensive cable model. This initial work considered only two-dimensional motion and steady-state wind conditions; however, turbulence was addressed later by DeLaurier.[3] The stability of the system was analyzed by showing that the motion decoupled into separate lateral and longitudinal motions. Lateral instabilities at low wind speeds were predicted (though later conversations with the author indicate these may have been caused by spurious results). Progress with the dynamics modeling of a tethered aerostat was made by Jones and Krausman[4] when a three-dimensional nonlinear dynamics model with a lumped mass discretized tether was established. Jones and DeLaurier[5] built on this basic model by introducing a segmented panel method for modeling the aerostat. This entailed dividing the aerostat into vertical slices to account for the effects of turbulence variations along the length of the hull. Another three-dimensional nonlinear dynamics model of a tethered aerostat was developed by Humphreys.[6] This model used a single partial differential equation to relate the motion and forces along the tether. Experimental validation of this dynamics model was achieved by performing tow tank tests with a scaled model.

In 1973, a linear model of a tethered aerostat was proposed by Redd et al.[7] Experimental data were used to validate their model in a steady wind. A study of the stability of the aerostat was performed, but the formulation of the linear model neglected the dynamic cross coupling of the tether and the aerostat. The nonlinear model developed by Jones and DeLaurier[5] was used by Badesha and Jones[8] to perform a linear stability analysis of a large commercial aerostat by linearizing the equations of motion of the nonlinear model. This analysis included only pendulum modes and neglected other modes of motion. The dynamics model developed by Badesha and Jones showed good agreement with experimental data as presented by Jones and Shroeder.[9] In 1998, Etkin[10] used a linear analysis to study the stability of a towed body. The stability of several different modes was studied as function of wind speed. Although the generalized formulation of this approach makes it relevant to a range of bodies constrained by a cable including that of a buoyant tethered aerostat in a flowfield, a detailed study of the dynamics of a specific tethered aerostat is necessary to establish confidence in the prediction of the behavior of the system.

The present work focuses on an investigation of the dynamics of a streamlined aerostat on a single tether using nonlinear modeling techniques and a linear stability analysis. The linearization of the system was performed using a finite difference approach rather than a conventional analytical method. The stability analysis includes several longitudinal and lateral modes and also considers the cross coupling between the tether and aerostat. Section II discusses the development of the nonlinear dynamics model of the cable and aerostat. In Section III, the nonlinear model is linearized numerically, and the effects on stability of changing the tether length are investigated.

II. Dynamics Model

A two-dimensional schematic of the system model, which consists of the tether and the aerostat, is shown in Fig. 1. The aerostat is modeled as a single body at the upper node of the tether, subject to buoyancy, aerodynamic drag, and gravity.

A. Dynamics of a Streamlined Aerostat

A model of the dynamics of a streamlined aerostat was developed to study its behavior in various wind conditions. The aerostat model is based on a streamlined aerostat manufactured by Aeros Flightcam of Canoga Park, California, as shown in Fig. 2. The central goal of this investigation is to study the stability of the aerostat on a single tether.

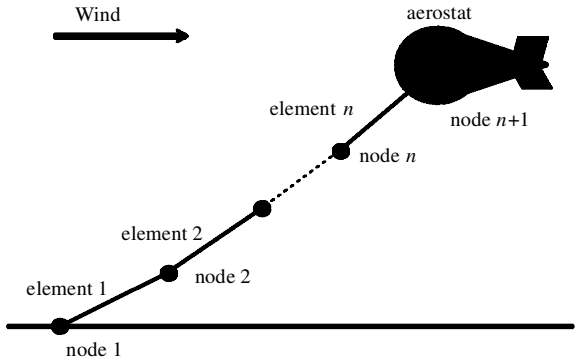

Fig. 1 Discrete implementation of tethered aerostat dynamics model.

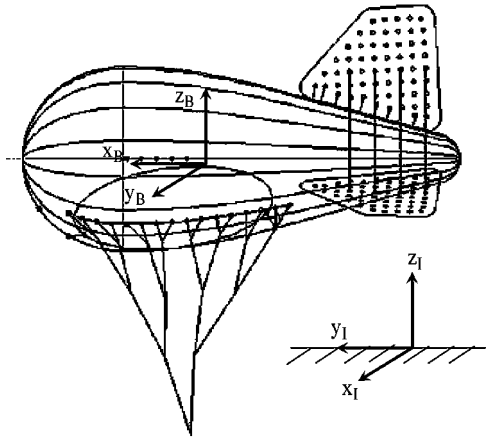

Fig. 2 Aeros Flightcam aerostat.

The parameters of interest of this study are the motion of the aerostat and the forces generated during its motion. The output of the simulation is the translational and rotational position and velocity of the aerostat as well as the tether tension while the input is a set of initial conditions and a wind field. The aerostat is considered to be rigid and is capable of full six degrees of freedom motion in three-dimensional space.

The methodology for the model development will be presented in two parts. The first is the derivation of the mathematical equations that govern the motion of the aerostat. The second part describes the process of determining the aerodynamic parameters of the aerostat.

1. *Equations of Motion*

The dynamic simulation of the aerostat is obtained by setting up and solving the equations of motion in three-dimensional space. The motion of the aerostat is described as the relative position and velocity of a body-fixed coordinate frame with respect to an inertial coordinate frame. The body frame is attached to the aerostat's center of gravity, and the inertial frame is fixed to an arbitrary point on the ground. A diagram illustrating the reference frames in relation to the aerostat is shown in Fig. 2. The translational motion is governed by Newton's Second Law and can be written as

$$\boldsymbol{F}_B = m\boldsymbol{a}_B \tag{1}$$

Because the aerodynamic forces will be calculated as components in the body frame, it becomes more convenient to solve for the motion variables also expressed in this frame. For this case the acceleration is found by differentiating the velocity with respect to the inertial frame $d\boldsymbol{V}_B/\boldsymbol{dt}$. This is related to $\partial \boldsymbol{V}_B/\partial t$, the rate of change of the velocity as seen in the body frame, as follows:

$$\frac{\boldsymbol{F}_B}{m} = \frac{\mathrm{d}\boldsymbol{V}_B}{\mathrm{d}t} = \frac{\partial \boldsymbol{V}_B}{\partial t} + \boldsymbol{\omega} \times \boldsymbol{V}_B \tag{2}$$

where $\boldsymbol{V}_B = [u \;\; v \;\; w]^T$ and $\boldsymbol{\omega} = [p \;\; q \;\; r]^T$ is the angular velocity of the aerostat. The rotational motion of the aerostat must satisfy Euler's equation:

$$\boldsymbol{M}_{\text{cm}} = \boldsymbol{I}\dot{\boldsymbol{\omega}} + \boldsymbol{\omega} \times \boldsymbol{I}\boldsymbol{\omega}, \qquad \boldsymbol{I} = \begin{bmatrix} I_{xx} & -I_{xy} & -I_{xz} \\ -I_{yx} & I_{yy} & -I_{yz} \\ -I_{zx} & -I_{zy} & I_{zz} \end{bmatrix} \tag{3}$$

where $\boldsymbol{M}_{\text{cm}}$ is the net external moment acting on the aerostat, taken about the mass center. Because of the symmetry of the aerostat in the x-z plane, the components I_{xy} and I_{yz} of the inertia tensor are zero.

The forces and moments that influence the aerostat are caused by one of the following sources: gravity, buoyancy, aerodynamics, and tether tension. The translational and rotational equations of motion of the aerostat can now be written as

$$\begin{aligned}
&(mg - F_b)\sin\theta + F_{Hx} + F_{Px} + F_{Sx} \\
&\quad + F_{Ux} + F_{tx} = m(\dot{u} + qw - rv) \\
&-(mg - F_b)\sin\phi\cos\theta + F_{Hy} + F_{Py} + F_{Sy} + F_{Uy} + F_{ty} \\
&\quad = m(\dot{v} + ru - pw) \\
&-(mg - F_b)\cos\phi\cos\theta + F_{Hz} + F_{Pz} + F_{Sz} + F_{Uz} + F_{tz} \\
&\quad = m(\dot{w} + pv - qu) \qquad (4) \\
&-z_b F_b \sin\phi\cos\theta + M_{Hx} + M_{Px} + M_{Sx} + M_{Ux} + M_{tx} \\
&\quad = I_{xx}\dot{p} - (I_{yy} - I_{zz})qr - I_{xz}(\dot{r} + pq) \\
&-x_b F_b \cos\phi\cos\theta - z_b F_b \sin\theta + M_{Hy} + M_{Py} + M_{Sy} \\
&\quad + M_{Uy} + M_{ty} = I_{yy}\dot{q} - (I_{zz} - I_{yy})pr - I_{xz}(r^2 - p^2) \\
&-x_b F_b \sin\phi\cos\theta + M_{Hz} + M_{Pz} + M_{Sz} + M_{Uz} + M_{tz} \\
&\quad = I_{zz}\dot{r} - (I_{xx} - I_{yy})pq - I_{xz}(\dot{p} - qr) \qquad (5)
\end{aligned}$$

where F_H, F_P, F_S, F_U, F_t and M_H, M_P, M_S, M_U, M_t are the aerodynamic force and moment contributions from the hull, port fin, starboard fin, upper fin, and tether and F_b is the buoyancy force applied in the positive z direction of the inertial frame. The position of the aerostat's center of buoyancy is given by x_b and z_b while mg is the weight of the aerostat acting in the negative z direction of the inertial frame. The left-hand side of the equations represents the external forces and moments acting on the aerostat, whereas the right-hand side represents the aerostat's motion.

2. *Component Breakdown Method*

The aerodynamic forces and moments on the aerostat are calculated by breaking down the aerostat into components with known aerodynamic characteristics. This approach is based on the method developed by Nahon for modeling of underwater vehicles.[11] The individual components are the hull, denoted with an H, and the three aft fins, denoted with an S, P, and U for the starboard, port, and upper fins, respectively. The method for calculating the effects of each component is as follows: 1) calculate the motion at a reference point on each component, 2) calculate the local angle of attack and sideslip angle, 3) calculate the lift and drag forces and moments, 4) transform these forces to the body frame, and 5) sum up the forces and moments.

To calculate the motion at a reference point on each component requires setting up a local frame on that component. The local frames for the hull and the three fins are located at their centers of pressure. The method for calculating the location of the center of pressure for the hull will be described in a later section.

3. *Aerodynamic Forces of the Fins*

For the fins the location of the center of pressure is taken to be at their $\frac{1}{4}$-chord line midway from the base to the tip. The velocity of the origin of the local frame of each fin with respect to the ground $\boldsymbol{V}_i$ can be found using the relationship:

$$\boldsymbol{V}_i = \boldsymbol{V}_B + \boldsymbol{\omega} \times \boldsymbol{r}_i \tag{6}$$

Once the velocity of the center of pressure of each component is known, the corresponding airspeed can be obtained from

$$\boldsymbol{U}_i = \boldsymbol{V}_i - \boldsymbol{W} \tag{7}$$

The local angle of attack α_i and sideslip angle β_i are calculated for each component using the relationships

$$\alpha_i = \tan^{-1}(w_i/u_i), \qquad \beta_i = \sin^{-1}(v_i/U_i) \tag{8}$$

where $U_i = \sqrt{(u_i^2 + v_i^2 + w_i^2)}$. For the vertical tail fin, definitions for the sideslip angle β and the angle of attack α are reversed because the fin is vertical rather than horizontal.

The fins are approximated as NACA 0018 airfoils, and the forces on each fin are characterized as lift L and drag D. The lift and drag forces for the fins are dimensionalized using the following equations:

$$L_i = \tfrac{1}{2}\rho A_f U_i^2 C_L, \qquad D_i = \tfrac{1}{2}\rho A_f U_i^2 C_D \tag{9}$$

where U_i is the local airspeed of each fin. The two-dimensional lift coefficient is assumed to depend linearly on the angle of attack for the region $0 < \alpha < \alpha_{\text{stall}}$, where α_{stall} is the stall angle. The region of the lift curve past the stall angle, $\alpha > \alpha_{\text{stall}}$, is taken to be flat with the lift coefficient retaining its maximum value. This is considered reasonable in the case of low-aspect-ratio airfoils.[12] The three-dimensional lift coefficient can be calculated for a particular aspect ratio using[13]

$$C_L = C_{L\alpha}\alpha, \qquad C_{L\alpha} = C_{l\alpha}\{A/(A + [2(A+4)/(A+2)])\} \tag{10}$$

The drag force on the fin is caused by parasitic drag and induced drag. The drag coefficient C_D is calculated by including both effects using the following equation:

$$C_D = C_{D0} + C_L^2 / \pi A e \tag{11}$$

It is important that if the airfoil has exceeded its stall angle the C_L used in this equation is calculated using the actual attack angle α to reflect the additional drag beyond the stall point.

Using these equations, the lift and drag forces are oriented according to the relative velocity of the fin. The lift force L_i is directed normal to the direction of motion, whereas the drag force D_i acts in the opposite direction of the velocity vector. For use with the equations of motion outlined earlier, these forces must be resolved into the aerostat's body frame. This can be achieved by first performing a simple rotation about the fin's local y axis. For inclusion with the rotational equations of motion, the resulting moment $\boldsymbol{M}_i$ is calculated as the cross product of the fin force vector $\boldsymbol{F}_i$ with a position vector from the center of mass of the aerostat to the centre of pressure of each fin as follows:

$$\boldsymbol{M}_i = \boldsymbol{r}_i \times \boldsymbol{F}_i \tag{12}$$

4. *Aerodynamic Forces of the Hull*

Using the method of Jones and DeLaurier,[5] the aerodynamic influence of the hull was estimated by a lift and drag force and a pitching moment. The lift force L_H and the drag force D_H are considered to be applied at the nose of the aerostat. The pitching moment about the nose M_{nose} accounts for the pitching tendencies of the aerostat. These quantities are calculated using the following equations:

$$\begin{aligned}
L_H &= q_0[(k_3 - k_1)\eta_k I_1 \sin(2\alpha)\cos(\alpha/2) + (Cd_c)_h J_1 \sin\alpha \sin|\alpha|] \\
D_H &= q_0[(Cd_c)_0 S_H \cos^2\alpha - (k_3 - k_1)\eta_k I_1 \sin(2\alpha)\cos(\alpha/2)] \\
M_{\text{nose}} &= -q_0[(k_3 - k_1)\eta_k I_3 \sin(2\alpha)\cos(\alpha/2) \\
&\quad + (Cd_c)_h J_2 \sin\alpha \sin|\alpha|]
\end{aligned} \tag{13}$$

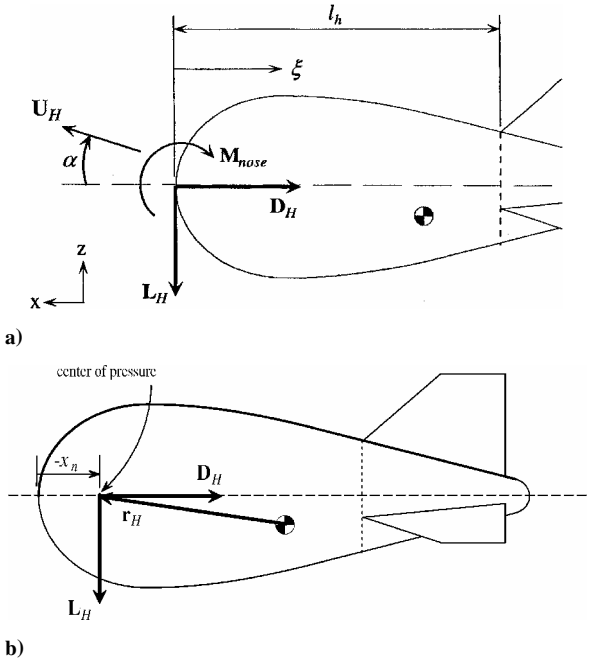

Fig. 3 Schematic of aerodynamic parameters of hull; a) original parameters and b) parameters with M_{nose} replaced by forces applied at center of pressure.

where $U_H = \sqrt{(u_H^2 + v_H^2 + w_H^2)}$ is the airspeed at the hull reference point. Also,

$$I_1 = \int_0^{l_h} \frac{\mathrm{d}A}{\mathrm{d}\xi}\,\mathrm{d}\xi = A_h \qquad \text{and} \qquad I_3 = \int_0^{l_h} \xi \frac{\mathrm{d}A}{\mathrm{d}\xi}\,\mathrm{d}\xi$$

$$J_1 = \int_0^{l_h} 2r\,\mathrm{d}\xi \qquad \text{and} \qquad J_2 = \int_0^{l_h} 2r\xi\,\mathrm{d}\xi \tag{14}$$

The values for I_1, I_3, J_1, and J_2 are based on the geometry of the aerostat. To utilize these equations, it is required to split the aerostat into two regions: the hull region, which extends from the nose to the starting point of the fins, and the fin region from this point to the tail. At $\xi = l_h$ the hull cross-sectional area is A_h. Figure 3 shows a two-dimensional diagram of the aerostat and the various aerodynamic parameters. The moment calculated about the nose M_{nose} of the aerostat is not appropriate for our simulation because the equations of motion sum the moments at the center of gravity of the aerostat.

To account for this, the force/moment system L_H, D_H, M_{nose} was replaced by an equivalent system at the aerostat's center of pressure. The center of pressure is the point at which the force/moment system has zero moment. It is located along the centerline of the aerostat at a distance from the nose, which is determined at each time step of the simulation. The distance from the nose to the center of pressure. x_n is calculated by equating M_{nose} to the moment generated about the nose by the lift force L_H using the following equation:

$$-M_{\text{nose}} = L_H(-x_n) \tag{15}$$

Using the convention of Jones and DeLaurier,[5] the orientation of the lift and drag forces on the hull follows a different convention from that of the fins. For the fins the forces are directed according the fin's motion, whereas the hull forces are directed according to its body axis independent of the direction of motion. The lift force acts perpendicular to the aerostat's central axis (x direction in the body frame) while the drag force acts in the negative x direction.

The configuration of the aerostat shown previously are for a two-dimensional representation. Figure 4 shows the motion variables

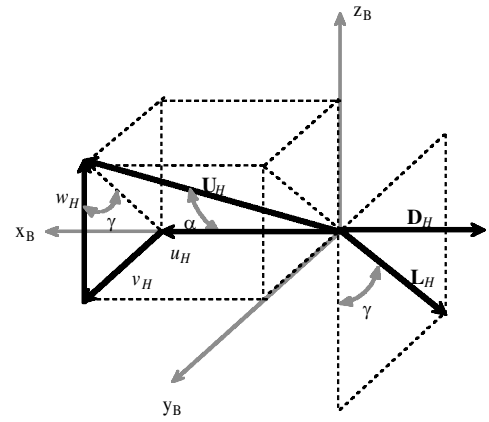

Fig. 4 Orientation of the hull motion and forces.

and hull forces for three-dimensional motion. The angle of attack of the hull α and the angle of the lift force in the y-z plane γ are found using the motion variables as follows:

$$\alpha = \cos^{-1}(u_H/U_H) \qquad \text{and} \qquad \gamma = \tan^{-1}(v_H/w_H) \tag{16}$$

To represent the aerodynamic forces in the body frame, the lift and drag forces are rotated by the angle γ. For the rotational equations of motion, the resultant moment $\boldsymbol{M}_H$ about the center of mass can be found using the equation

$$\boldsymbol{M}_H = \boldsymbol{r}_H \times \boldsymbol{F}_H \tag{17}$$

Added mass is included in the analysis for the hull by defining the effective mass of the aerostat m_e as the sum of the true mass m and the added mass m_a as follows:

$$m_e = m + m_a \tag{18}$$

where $m_a = k_i \rho V$ and k_i is the added mass coefficient[14] in the appropriate direction.

B. Tether Model

The tether is used to constrain the motion of the aerostat, and this must be accounted for in the dynamics model by combining the aerostat and tether models. This work uses a lumped-mass model of the tether in order to model its dynamic behavior. In this type of model, which is discussed in more detail by Driscoll and Nahon,[15] the continuous cable is first discretized into elements. The mass of each element is lumped at its endpoints (called nodes). The internal stiffness and damping characteristics of the cable are modeled as lumped parameter stiffness and damping elements connecting those nodes. This type of model, shown in Fig. 5, has been validated for a variety of underwater systems with excellent agreement with in-field measurements.[15]

The position of each node is described with respect to an inertial reference frame by a three-component vector $\boldsymbol{p}_i = [x_i \;\; y_i \;\; z_i]^T$. Each cable element is considered to be a straight elastic element, subject to forces at its endpoints. This method of modeling allows each cable element to possess distinct properties, such as density and stiffness. The orientation of each cable element is represented using a Z-Y-X (ψ, θ, ϕ) Euler angle set. Because the torsion of the cable is not included in the model, the ψ rotation about the inertial Z axis is constrained to zero. The Euler angles θ_i and ϕ_i can be calculated from the coordinates of the appropriate nodal endpoints.[15]

1. *Internal Forces*

The internal forces acting within an element are caused by its viscoelastic properties. These are represented schematically in Fig. 5. The tension in the cable caused by its structural stiffness is considered to act only in the tangential direction and is modeled by a

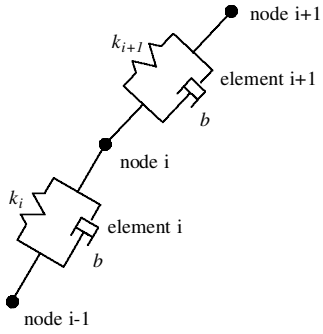

Fig. 5 Schematic of viscoelastic internal forces for the tether model.

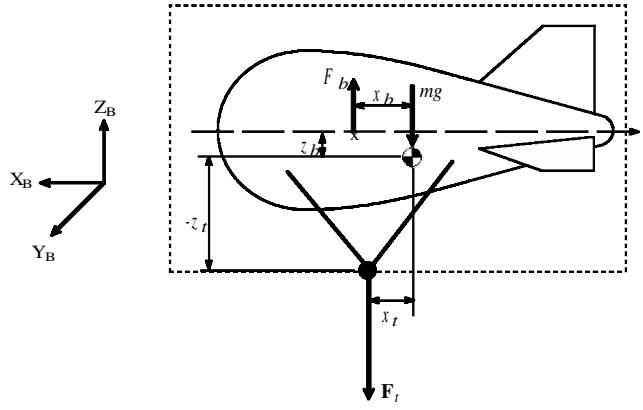

Fig. 6 Connection point of tether and aerostat.

linear tension-strain relationship. The friction between the braids of the cable tends to create a damping effect. This effect is assumed to be linear with the strain rate. The total tension in a cable element as a result of these effects is therefore written as

$$T_i = A_t E\varepsilon + b\varepsilon, \qquad \varepsilon = \left(l_i - l_i^u\right)/l_i^u \tag{19}$$

2. External Forces

The external forces acting on the cable element are those caused by aerodynamic drag and gravity. The drag force acting on the cable element can be calculated according to Morison's equation

$$D_t = \tfrac{1}{2}\rho C_d d_t l_i^u \|\boldsymbol{u}_i\|^2 \tag{20}$$

The velocity u_i accounts not only for the motion of the cable element, but also the motion of the surrounding air, that is, $\boldsymbol{u}_i = \boldsymbol{p}_i - \boldsymbol{W}$. The drag coefficient is modified by loading functions,[15] which account for the nonlinear breakup of drag between the normal and tangential directions. Once the drag for elements i and $i+1$ are calculated, half of each value is applied to the ith node, which joins the two elements. Finally, the gravitational force acting on a cable element is applied, based on the element's density and volume.

3. Tether Attachment Point

The coupling of the tether model and the aerostat model was achieved by connecting the uppermost node of the tether to the base of the aerostat's flying lines, as shown in Fig. 6. The aerostat and its flying lines (everything within the dashed box) are treated as a single rigid body. Hence, the two flying lines shown can be interpreted as rigid members. In reality, for an aerostat of this type many flying lines would be present and arranged in a harness (see Fig. 2) in order to rigidly secure the aerostat. It would be difficult to incorporate the effects of the flexibility of a complex harness, and therefore the rigid-body approximation is deemed adequate for this level of investigation. The force from the top node of the tether $\boldsymbol{F}_t$ is included in the equations of motion of the aerostat. For the rotational equations of motion, the moment from the tether force is calculated using

$$\boldsymbol{M}_t = \boldsymbol{r}_t \times \boldsymbol{F}_t \qquad \text{where} \qquad \boldsymbol{r}_t = \begin{bmatrix} x_t \\ 0 \\ z_t \end{bmatrix} \tag{21}$$

The actual location of the attachment point relative to the aerostat can have a significant effect on the behavior of the aerostat. Aeros Flightcam offered some general insights as to where to place the tether attachment point, based on their experience with tethered aerostats. It was recommended that, in the interests of stability, the aerostat should have a pitched-up attitude of about 5 to 10 deg and that the vertical distance of the attachment point from the aerostat centerline z_t should be about $1\frac{1}{2}$ times the aerostat diameter.

The distance x_t was calculated to yield the selected pitch angle by summing the moments about the aerostat's center of mass in a zero wind equilibrium position, as follows:

$$-F_b x_b \cos\theta_0 + F_b z_b \sin\theta_0 + F_t x_t \cos\theta_0 - F_t z_t \sin\theta_0 = 0 \tag{22}$$

which can be rearranged as

$$\tan\theta_0 = \frac{F_b x_b - F_t x_t}{F_b z_b - F_t z_t} \tag{23}$$

In the absence of wind, the buoyancy force F_b and the tether force F_t both act along the z direction of the Earth-fixed inertial frame. These two forces along with the position of the center of buoyancy x_b and z_b are all fixed quantities for the aerostat. Therefore, once values for two of the other three remaining variables θ_0, x_t, and z_t are selected this equation can be used to solve for the remaining variable. For our purposes we selected a certain pitch angle θ_0 and vertical tether attachment position z_t and solved for the unknown horizontal tether attachment position x_t.

C. Physical Parameters

To solve the equations of motion outlined earlier, it is necessary to define numerous physical parameters for this particular aerostat. The relevant geometric properties of the Aeros aerostat are given in Table 1. There is an internal air envelope used to regulate helium pressure known as the "ballonet". This is achieved by venting and accumulating air using electric blowers. The blowers are located at the base of the belly where the ballonet meets the hull. The tail fins are made from the same material as the hull and are inflated with helium. Multiple strands of nylon cord connect the face of each fin to the face of the adjacent fin. The nylon cord is cinched tight, and the tension in the cords keeps the fins in place. The fins are arranged in an inverted Y configuration. The two dihedral fins are offset by an angle of 112.5 deg from the vertical fin.

To obtain the physical parameters of the aerostat, a three-dimensional CAD model was generated using PRO-E. The CAD model was constructed to represent accurately the actual aerostat, complete with a thin-walled shell of the hull and ballonet envelopes, solid models of the gases contained within, and a plate that houses the blowers. The appropriate density was assigned to each part, and the various physical parameters were computed by PRO-E. The mass and volume of the relevant parts are given in Table 1. Other parameters of interest obtained in this manner are the location of the aerostat's center of buoyancy, the center of mass, and the inertia tensor. The center of buoyancy was found by obtaining the center of mass for a solid, homogenous aerostat with the proper dimensions. From Table 1 it is noted that the mass of the gases are a significant contribution to the overall mass of the aerostat. When modeling lighter-than-air vehicles, it is essential to account for the mass of these internal gases when determining any physical parameters.

1. Aerodynamic Parameters

The aerodynamic parameters used in the dynamics model must be estimated for this particular aerostat. The location of the center of pressure for each component was calculated using the explanation

Table 1 Physical parameters of Aeros aerostat

Parameter	Value
Aerostat length, L	18.3 m
Helium volume	467.1 m^3
Ballonet volume	52.2 m^3
Total volume	519.3 m^3
Helium mass	78.9 kg
Air mass	64.2 kg
Hull mass	115.6 kg
Ballonet mass	25.6 kg
Blowers mass	10.0 kg
Tail fin mass (all 3)	63.6 kg
Total mass	357.9 kg
Density of air	1.229 kg/m^3
Density of helium	0.169 kg/m^3
Buoyancy	6,260.7 N
Net lift	2,749.7 N
Aerostat diameter, D	7.7 m
Center of mass (from nose)	
x_{cm}	−8.476 m
y_{cm}	0
z_{cm}	−0.491
Center of buoyancy (from c.m.)	
x_b	0.710 m
y_b	0
z_b	0.524 m
Inertia tensor components	
I_{xx}	3,184 kg . m^2
I_{yy}	10,011 kg . m^2
I_{zz}	9,808 kg . m^2
$I_{xz} = I_{zx}$	−641 kg . m^2

given earlier and is listed in Table 2. All distances given are measured from the aerostat's center of mass.

As noted earlier, the aerostat was split into two regions: the hull region, which includes everything from the nose to the start of the fins, and the fin region, which includes the fins and the section of the hull behind the start of the fins. The area for each fin A_f is the cross-sectional area from the centerline of the aerostat to the tip of the fin. The aspect ratio of the fins is defined as the square of the distance from the aerostat's centerline to the fin tip divided by A_f. The value of $C_{L\alpha}$ takes into account losses arising from the fins' location at the rear of the vehicle. The flowfield in the vicinity of the fins will have experienced disruptions from passing over the hull, resulting in a reduction of the fins' capability to produce lift.

The added mass coefficients k_1 and k_3 were estimated using data for ellipsoids.[13] The hull efficiency factor η_k was found by averaging values given for three different aerostats from Jones and DeLaurier.[5] The crossflow drag coefficient for the hull $(Cd_c)_h$ was estimated using the drag coefficient for a cylinder. The estimation of the zero-angle axial drag $(Cd_h)_0$ was based on the drag coefficient for a streamlined shape with a fineness ratio of 2.4 (Ref. 15), where the fineness ratio is the length of the body divided by its maximum diameter. The hull reference area S_H is defined as the (hull volume)$^{2/3}$. The evaluation of the integral for I_1 gives the cross-sectional area of the hull at the hull fin region boundary A_h. The integral for J_1 is equivalent to the cross-sectional area of the hull region of the aerostat in the xz plane, which was found using the evaluation tools of PRO-E on the CAD model. To obtain the integrals for I_3 and J_2, the hull profile was approximated by a 10th-order polynomial, and the integrals given in Eq. (14) were then evaluated numerically.

2. *Tether Properties*

The tether that was modeled has physical parameters listed in Table 3. The Plasma tether is manufactured by Puget Sound Rope. The manufacturer provided the data for the density and strength of the cable. The damping ratio and elastic modulus were estimated from experimental tests performed on a sample of Plasma tether. The damping coefficient b used in the tether model is calculated using the following equation:

$$b = \zeta b_c \tag{24}$$

Table 2 Aerodynamic parameters of Aeros aerostat

Parameter	Value
Center of pressure	
Hull	
x_h	8.476 − x_n
y_h	0
z_h	0.491 m
Vertical fin	
x_v	−4.92 m
y_v	0
z_v	3.74 m
Port fin	
x_p	−4.92 m
y_p	2.98 m
z_p	−0.706
Starboard fin	
x_s	−4.92 m
y_s	−2.98 m
z_s	−0.706
Fins	
A_f	30.0 m^2
A	2.18
$C_{L\alpha}$	2.0
C_{D0}	0.012
α_{stall}	11.0 deg
Hull	
k_1	0.16
k_3	0.76
η_k	1.2714
$(Cd_c)_h$	0.28
$(Cd_h)_0$	0.0394
S_H	59.35 m^2
I_1	20.43 m^2
I_3	−170.51 m^3
J_1	75.84 m^2
J_2	433.85 m^3

Table 3 Tether parameters

Parameter	Value
Diameter, d_t	6 mm
Density, ρ_t	840 kg/m^3
Elastic modulus, E	37.4 GPa
Damping ratio, ζ	0.017

III. Linear Stability Analysis

The nonlinear dynamics model of the streamlined aerostat on a single tether is useful for obtaining time histories of the aerostat's motion in response to a particular wind input. However, in order to acquire a quantitative assessment of the stability of the aerostat a linear approximation of the system was derived, and its eigenvalues and eigenvectors were studied.

The nonlinear dynamics simulation can be thought of as a set of functional relationships where the derivative of each state variable is dependent on the full set of state variables. This is demonstrated by the following equation:

$$\boldsymbol{X} = \boldsymbol{F}(\boldsymbol{X}) \tag{25}$$

where $\boldsymbol{X} = [x_1, \dot{x}_1, y_1, \dot{y}_1, z_1, \dot{z}_1, \ldots, x_n, \dot{x}_n, y_n, \dot{y}_n, z_n, \dot{z}_n, \phi, \dot{\phi}, \theta, \dot{\theta}, \psi, \dot{\psi}]^T$ is the state vector. It contains the position and velocity of all elements of the model, with respect to the inertial frame. This includes each of the tether nodes as well as the aerostat. For the aerostat node there are an additional six state variables representing its angular position and velocity. Therefore, the total number of state variables is $6n + 6$, where n is the number of tether nodes. There are no state variables for the bottom-most tether node because it is fixed to the ground; hence, the translational variables with the subscript n represent the aerostat node.

A. Linear Model

Linearizing Eq. (25) leads to

$$\dot{\boldsymbol{X}} = \boldsymbol{A}\boldsymbol{X} \tag{26}$$

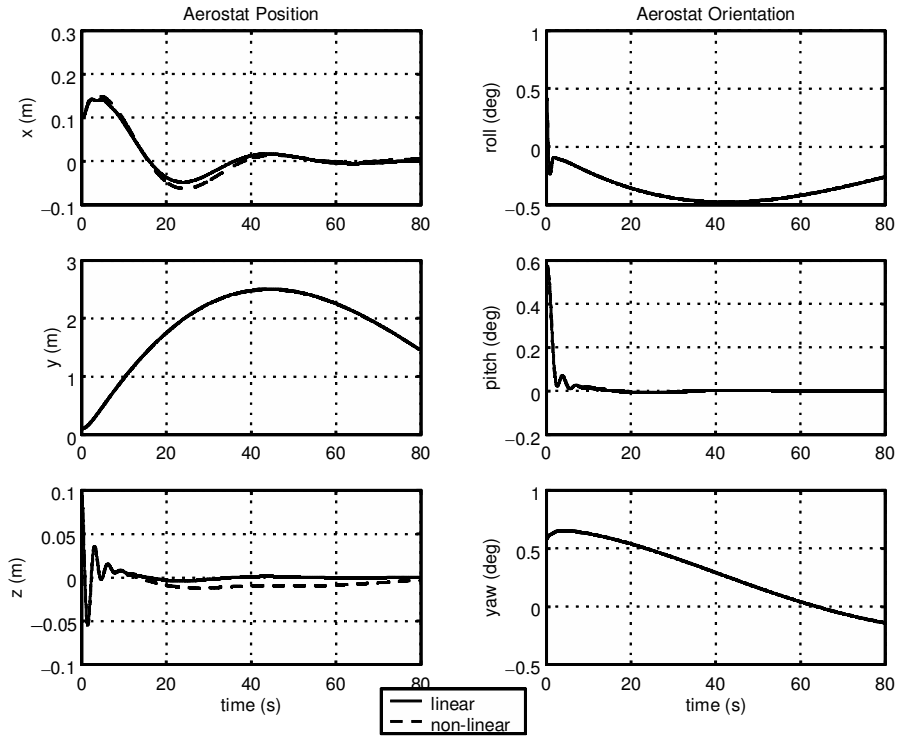

Fig. 7 Comparison of linear and nonlinear simulation results of aerostat motion for case with single tether of $L_t = 300$ m and wind speed $W = 10$ m/s.

where the state matrix $\boldsymbol{A}$ is defined as

$$\boldsymbol{A} = \frac{\partial \boldsymbol{F}}{\partial \boldsymbol{X}} = \begin{bmatrix} \frac{\partial f_1}{\partial x_1} & \frac{\partial f_1}{\partial x_1} & \cdots & \frac{\partial f_1}{\partial \psi} \\ \frac{\partial f_2}{\partial x_1} & \frac{\partial f_2}{\partial x_1} & \cdots & \frac{\partial f_2}{\partial \psi} \\ \vdots & \vdots & \ddots & \vdots \\ \frac{\partial f_{6n+6}}{\partial x_1} & \frac{\partial f_{6n+6}}{\partial x_1} & \cdots & \frac{\partial f_{6n+6}}{\partial \psi} \end{bmatrix} \tag{27}$$

where $\boldsymbol{F} = [f_1 \;\; f_2 \;\; \cdots \;\; f_{6n+6}]^T$. The most direct method for obtaining the state matrix is to perform a numerical differentiation by finite difference of the nonlinear differential equations. The first step is to choose a reference equilibrium condition about which the system will be linearized. Next, each state variable is perturbed slightly from its equilibrium value. The ensuing response of every state variable is observed and compared to its equilibrium value. The difference between the response and the equilibrium value is divided by the perturbation to approximate each element of the state matrix. For example, in the case of the first element in the first row, we have

$$\frac{\partial f_1}{\partial x_1} \approx \frac{f_1' - f_{1_0}}{\Delta x_1} \tag{28}$$

where f_1' is the value of f_1 following a perturbation of a particular state variable (in this case, x_1), whereas f_{1_0} is the value of f_1 at the reference equilibrium condition and Δx_1 is the perturbation value of x_1. The value for the perturbation is typically very small (10^{-5} was used). The reference equilibrium condition is one in which the tethered aerostat system is in a steady-state wind field in the absence of turbulence. The process can be repeated for a variety of wind speeds in the range of interest.

Once $\boldsymbol{A}$ is formed, it is necessary to verify its validity through a comparison of the linear and nonlinear responses to a specified initial condition. MATLAB® was used to obtain the linear response. The nonlinear response was obtained using the nonlinear dynamics model described in the preceding section. All six position variables for the aerostat were simultaneously given an initial perturbation from the equilibrium condition. The perturbation was 0.1 m for the translational variables and 0.01 rad for the rotational variables. The linear and nonlinear responses for the position variables are shown in Fig. 7. The good agreement between the two responses demonstrates the success of the linearization process and provides justification for pursuing the linear stability analysis.

1. *Decoupling*

The stability of vehicle models is typically analyzed by decoupling the motion variables into lateral and longitudinal subsets. The longitudinal variables are defined as translational motion in the x and z directions and rotational motion about the y axis (i.e., $x_{1\ldots n}$, $x_{1\ldots n}$, $z_{1\ldots n}$, $z_{1\ldots n}$, θ, θ). The lateral variables are defined as translational motion in the y direction and the rotational motion about the x and z axes (i.e., $y_{1\ldots n}$, $y_{1\ldots n}$, ϕ, ϕ, ψ, ψ). For a tethered aerostat symmetrical about the x-z plane, it can be shown that longitudinal and lateral decoupling will occur. To ensure that this holds true for our tethered aerostat system, the state vector and the state matrix were rearranged to separate the longitudinal and lateral systems. The new state vector $\boldsymbol{X}'$ is as follows:

$$\boldsymbol{X}' = \begin{bmatrix} \boldsymbol{X}_{\text{long}} \\ \boldsymbol{X}_{\text{lat}} \end{bmatrix}, \qquad \boldsymbol{X}_{\text{long}} = \begin{bmatrix} x_1 \\ x_1 \\ z_1 \\ z_1 \\ \vdots \\ z_n \\ \theta \\ \theta \end{bmatrix}, \qquad \boldsymbol{X}_{\text{lat}} = \begin{bmatrix} y_1 \\ y_1 \\ \vdots \\ y_n \\ \phi \\ \phi \\ \psi \\ \psi \end{bmatrix} \tag{29}$$

To be consistent with the new arrangement of $\boldsymbol{X}'$, the state matrix $\boldsymbol{A}$ must be rearranged by exchanging the appropriate row and column for each variable that was repositioned. Once this process is complete, we can determine whether the longitudinal and lateral variables are, in fact, decoupled. If the longitudinal and lateral systems are decoupled, the new state matrix $\boldsymbol{A}'$ will be partitioned into

four distinct submatrices: a longitudinal submatrix $\boldsymbol{A}_{\text{long}}$, and a lateral submatrix $\boldsymbol{A}_{\text{lat}}$, as well as two null submatrices. The dimensions and location of each submatrix are as follows:

$$\boldsymbol{A}' = \begin{bmatrix} [\boldsymbol{A}_{\text{long}}]_{(4n+2)\times(4n+2)} & [\boldsymbol{0}]_{(4n+2)\times(2n+4)} \\ [\boldsymbol{0}]_{(2n+4)\times(4n+2)} & [\boldsymbol{A}_{\text{lat}}]_{(2n+4)\times(2n+4)} \end{bmatrix} \tag{30}$$

For our system it was found that the lower left matrix was in fact comprised of all zeros; however, the upper-right submatrix matrix had several elements with small magnitudes. Because these values were quite small (the largest being on the order of 10^{-4}) compared to the magnitude of the elements of the other matrices (the largest being on the order of 10^4), it can be concluded that the motion is essentially decoupled. Therefore, the system can be analyzed as two separate systems as follows:

$$\boldsymbol{X}_{\text{long}} = \boldsymbol{A}_{\text{long}}\boldsymbol{X}_{\text{long}}, \qquad \boldsymbol{X}_{\text{lat}} = \boldsymbol{A}_{\text{lat}}\boldsymbol{X}_{\text{lat}} \tag{31}$$

2. Eigenvalues and Eigenvectors

The aerostat's natural motion and stability are characterized by the eigenvalues and eigenvectors of the corresponding state matrix. Each eigenvalue (or pair of eigenvalues) represents a particular mode of the motion, while its corresponding eigenvector provides the relationship of each state variable in that mode. Eigenvalues can exist either as complex conjugates denoted as $\lambda_{1,2} = \sigma \pm \omega_d i$ or as distinct real numbers. A complex conjugate pair of eigenvalues indicates that the mode is oscillatory, and a real eigenvalue indicates nonoscillatory motion. For stability of the system, all of the real parts of the eigenvalues must be negative. The damped frequency ω_d is the imaginary part of the eigenvalue, and the natural frequency and damping ratio are found from

$$\omega_n = \sqrt{\sigma^2 + \omega_d^2}, \qquad \zeta = \sin\theta = -\sigma/\omega_n \tag{32}$$

Each eigenvalue of a complex conjugate pair has a conjugate that is a reflection about the real axis. Both eigenvalues correspond to a single mode with a particular frequency and damping ratio.

Each element of the corresponding eigenvector represents the magnitude and phase of the response of a particular state variable. If phasor representation is used to display the elements of the eigenvectors, the radius corresponds to the magnitude of the response, and the angle corresponds to the phase. The magnitude and phase of the state variables obtained from the eigenvectors are relative to each other and are not absolute. In the case of complex conjugate eigenvalues, the corresponding eigenvectors consist of complex conjugates mirrored about the real axis.

B. Results

The cable was discretized into 10 elements, yielding longitudinal and lateral subsystems of order 42 and 24, respectively. MATLAB® was used to compute the eigenvalues and eigenvectors for $\boldsymbol{A}_{\text{long}}$ and $\boldsymbol{A}_{\text{lat}}$. Because the number of modes was large (a total of 33), we chose to only study the four lowest frequency modes in each subsystem because the high-frequency modes are not likely to yield significant motion in the actual system.

The results for a baseline case are presented in Fig. 8. The conditions for this case are tether length $L_t = 300$ m with a steady-state pitch angle $\theta_0 = -4$ deg (pitched nose up). All other physical parameters correspond to the values presented for the Aeros Aerostat in Sec II. The wind model used had a wind speed constant with height. The four longitudinal and four lateral modes considered here were found to be stable over the full range of wind speeds. The remaining modes omitted from the presentation were observed to be stable as well.

To gain a better appreciation of the results, the eigenvectors for each of the modes were studied in attempt to classify the motion. Details of the classification of each lateral mode are as follows:

1) In the pendulum mode the eigenvectors for the position and velocity of the tether nodes in the y direction, $y_{1\ldots n}$ and $\dot{y}_{1\ldots n}$, are 90 deg out of phase, and the amplitudes of both motion variables increase linearly from the base to the top of the tether. The magnitude of the yaw rotation ψ of the aerostat is appreciable, which suggests that yawing motion is coupled with the pendulum oscillation. This mode has by far the lowest frequency, which is expected for the pendulum mode, considering the size of the system. The dramatic increase in period with wind speed at $W = 2$ m/s is likely caused by the coupling of the pendulum motion and the yawing of the aerostat. The effects of this phenomenon appear to become saturated at $W = 4$ m/s. As the wind speed increases beyond 6 m/s, the period decreases gradually, suggesting that the wind eventually overcomes this coupling. At these higher speeds the lateral pendulum mode behaves more like the longitudinal pendulum mode, which decreases with wind speed. For wind speeds below 2 m/s, the eigenvector element representing the yaw of the aerostat is about 270 deg out of phase with the aerostat's lateral position element. For wind speeds beyond 4 m/s, the phase angle is between 55 and 90 deg. The shift in phase is observed to increase dramatically the period of the pendulum mode. This illustrates the importance of including the cross coupling between the tether and aerostat in the dynamic analysis.

2) In the rolling mode the dominant motion is the rolling of the aerostat as large relative amplitudes of the roll angle ϕ and rotational velocity $\dot{\phi}$ are observed.

3) With the first tether harmonic the eigenvectors for the position and velocity of the tether nodes are 90 deg out of phase. The magnitude of the position of the tether nodes is a maximum at the middle node, which corresponds to a simple concave/convex shape.

4) With the second tether harmonic the position and velocity of the tether nodes are 90 deg out of phase. The motion for the nodes under node 5 and above node 5 are 180 deg out of phase. The magnitude of the position of the tether is a maximum at nodes 2 and 7 and is a minimum at node 5, which corresponds to an S-shaped tether. As expected, the frequency of this mode is twice as high as the first tether harmonic.

Classification of the longitudinal eigenvectors followed a similar process. The characteristics and classification of the four lowest frequency longitudinal modes are as follows:

1) For the pendulum mode the dominant motion variables are the position and velocity of the tether nodes in the x direction, $x_{1\ldots n}$ and $\dot{x}_{1\ldots n}$. The motion in the z direction is negligible. The eigenvectors corresponding to $x_{1\ldots n}$ and $\dot{x}_{1\ldots n}$ are 90 deg out of phase. The amplitudes of $x_{1\ldots n}$ and $\dot{x}_{1\ldots n}$ increase linearly from the base to the top of the tether.

2) For the pitching mode the dominant motion is the pitching of the aerostat as large relative amplitudes of the pitch angle θ and rotational velocity $\dot{\theta}$ are observed.

3) For the axial spring mode the dominant motion variables are the position and velocity in z direction, $z_{1\ldots n}$ and $\dot{z}_{1\ldots n}$. The magnitudes of the motion variables in the x direction are negligible.

4) For the first tether harmonic mode, like the pendulum mode, the dominant motion variables are the position and velocity of the tether nodes in the x direction, whereas the motion in the z direction is negligible. The magnitude of the x position of the tether nodes is a maximum at the middle node, which corresponds to a simple concave/convex shape.

1. Reference Frequencies

The basic motion characteristics from the linear analysis can be compared with the analytical solutions for an idealized tethered aerostat, as a means of checking the validity of the dynamics model. The analytical reference frequencies for the motion of a buoyant mass on a string are obtained as follows:

For the pendulum mode:

$$\omega_n = \sqrt{\frac{F_b - mg}{m_e L_t}} \tag{33}$$

For the axial spring mode:

$$\omega_n = \sqrt{E A_t / m_e L_t} \tag{34}$$

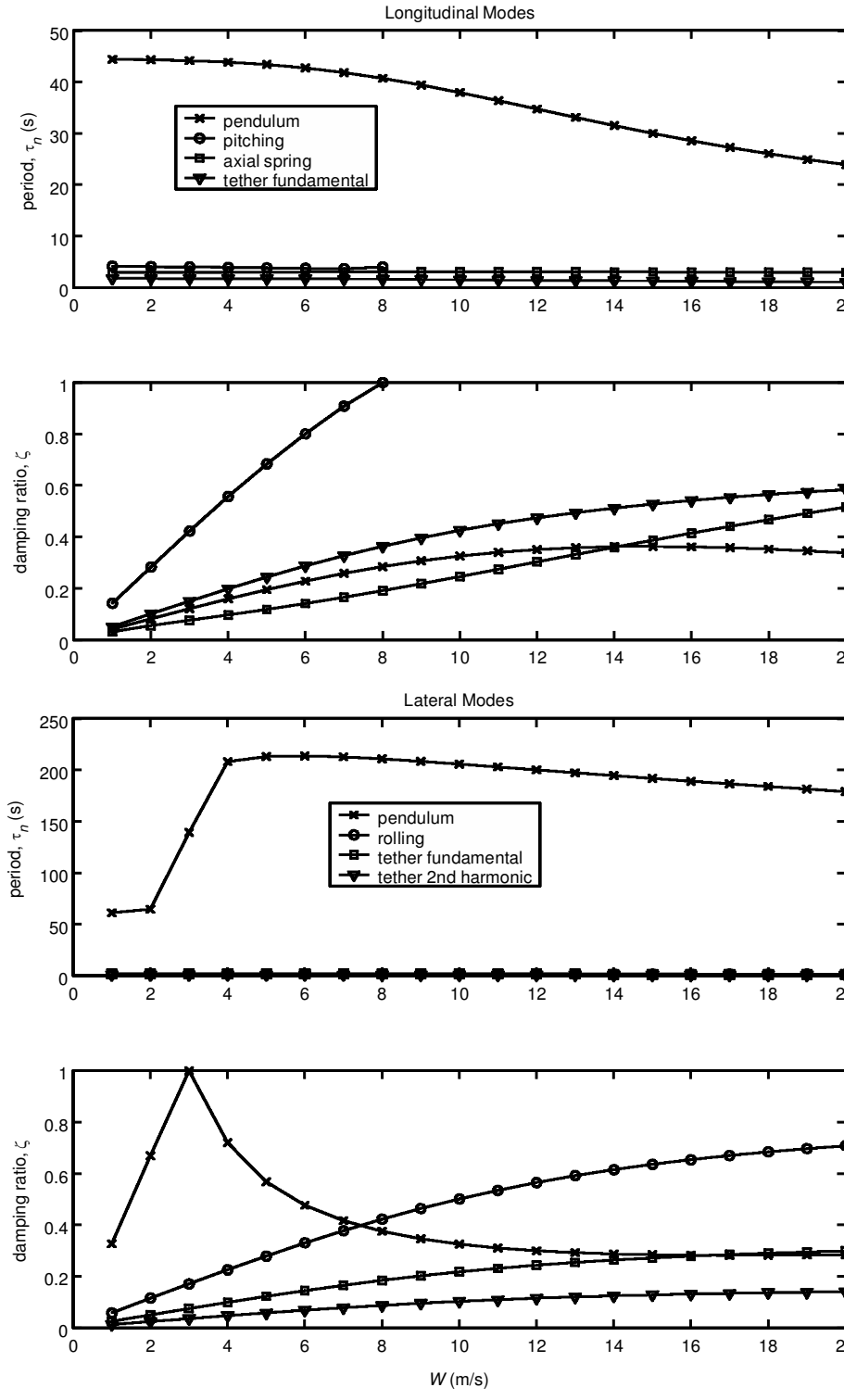

Fig. 8 Longitudinal and lateral modes for baseline case with $L_t = 300$ m and $\theta_0 = -4$ deg.

for the tether's transverse mode for the nth harmonic[16]:

$$\omega_n = \frac{n\pi}{L_t}\sqrt{\frac{F_b - mg}{\rho_t A_t}} \qquad n = 1, 2, \ldots \tag{35}$$

For the pendulum modes the relevant effective mass for the longitudinal case is in the x direction, and for the lateral case it is in the y direction. For the axial spring mode the effective mass in the z direction is used. For the transverse modes added mass is not included in determining the net lift of the aerostat given as $F_b - mg$ because the added mass only applies to the inertial properties of the aerostat. The theoretical natural frequencies are used to find the theoretical periods of each mode using $\tau_n = 2\pi/\omega_n$. The results are presented in Table 4 and compared to the periods given in Fig. 8 from the linear analysis at $W = 1$ m/s.

For the fundamental transverse tether mode the observed frequencies from the linear model were identical for both the longitudinal and lateral cases. Close agreement is observed for all modes with the exception of the lateral pendulum, which has a difference of 7.2% with the theoretical value. This discrepancy could be attributed to the fact that the comparison uses the results from the linear model at $W = 1$ m/s, whereas the theoretical period

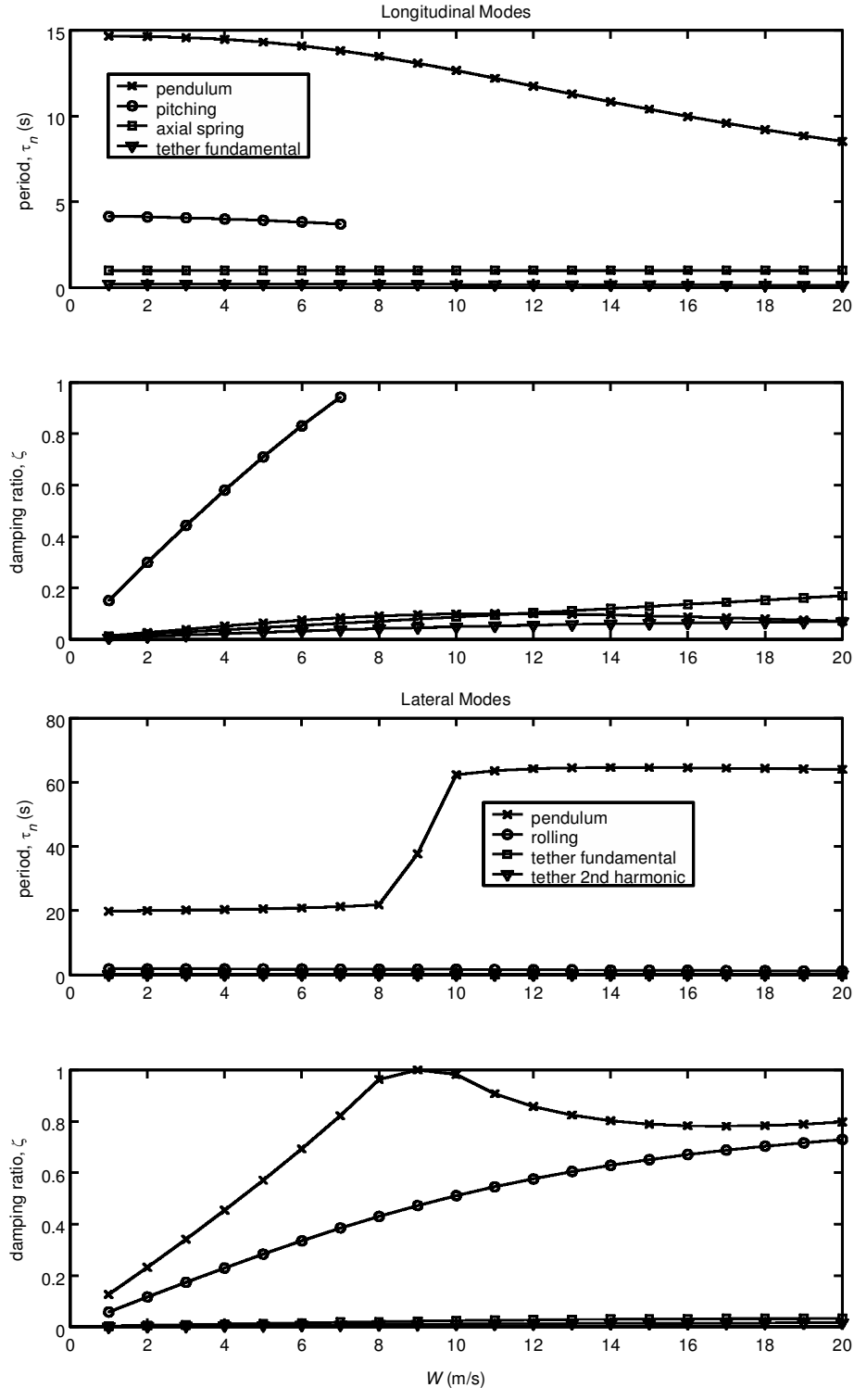

Fig. 9 Longitudinal and lateral modes for case with $L_t = 33.3$ m and $\theta_0 = -4$ deg.

corresponds to a system with $W = 0$. Overall, the good agreement between the linear model and the theoretical oscillations provides a first level of assurance of the general validity of the dynamics model.

2. *Changing the Tether Length*

To assess the system's sensitivity to changes in tether length, the stability of the system with different tether lengths was investigated. In the target application of supporting a telescope receiver, the tether will likely be shorter than the 300 m used in the baseline case. Therefore, the behavior of the aerostat with shorter tether lengths of $L_t = 100$ and 33.3 m was studied. The results for $L_t = 33.3$ m are given in Fig. 9. Significant differences were found in the behavior of the system as the tether length was decreased. For the longitudinal modes the pendulum, axial spring, and fundamental tether modes all experience a reduction in damping as tether length shortens. Laterally, there is also a reduction in the damping of the transverse tether modes. There is little change observed in the two aerostat rotational modes, which is expected because the motion of these modes pertain primarily to the aerostat and are therefore independent of the tether length.

Table 4 Comparison of theoretical and linear model results for period τ_n of certain oscillatory modes for baseline case

Model type	Longitudinal pendulum	Lateral pendulum	Axial spring	First tether harmonic	Second tether harmonic
Theoretical	43.9 s	58.0 s	2.96 s	1.81 s	0.90 s
Linear model	44.4 s	62.2 s	2.96 s	1.78 s	0.90 s
% Difference	1.1	7.2	≈ 0	1.7	≈ 0

It appears that the reduction in damping ratio for the tether modes (i.e., axial spring, tether harmonics) is the result of losing the majority of the damping influence from the wind. For the case with $L_t = 300$ m, the damping of each tether mode increases appreciably as wind speed increases, but for the case with $L_t = 33.3$ m the damping ratio experiences a much smaller increase as W increases. With a shorter tether there is less material present to be affected by the wind's influence. Based on these results, it would appear that the system in general is more stable with longer tether lengths.

There is also a distinct difference between the characteristics of the lateral pendulum mode for the two cases with different tether length. The shift to a lower-frequency oscillation occurs at a higher wind speed for the shorter tether. Also, the damping for the short tether case experiences a more gradual change and declines to a much higher steady-state value at high wind speeds. This suggests that the lateral pendulum motion for tethered the aerostat is more stable with the shorter tether at high wind speeds. For low wind speeds ($W < 4$ m/s) the stability of this mode is better with the longer tether length of $L_t = 300$ m.

IV. Conclusions

A nonlinear model of a tethered aerostat was developed, based on a lumped-mass approach for the tether, and a component breakdown approach for the aerostat. This model was then linearized to allow an examination of the stability of the tethered aerostat in various winds. The behavior observed at low wind speeds correlated well with analytical predictions. It was found that the system remained stable at all wind speeds and that the stability improved with increasing wind speed for all modes of motion with the exception of the lateral pendulum mode. The stability of this mode increases with an increase in wind speed until a certain critical point after which the stability decreases eventually reaching a steady state. It was also found that all modes of the system, again with the exception of the lateral pendulum mode, became more stable with the longer tether. The lateral pendulum mode has better stability with the longer tether at low wind speeds; however, at high wind speeds it appears more stable with the shorter tether.

Acknowledgments

The authors would like to thank staff at the National Research Council of Canada and at Worldwide Aeros for their technical support. Funding for this work was received from Natural Sciences and Engineering Research Council of Canada, the Canada Foundation for Innovation, and the British Columbia Science Council.

References

[1]Legg, T. H., "A Proposed New Design for a Large Radio Telescope," *Astronomy and Astnophysics Supplement Series*, Vol. 130, 1998, pp. 369–379.

[2]DeLaurier, J. D., "A Stability Analysis for Tethered Aerodynamically Shaped Balloons," *Journal of Aircraft*, Vol. 9, No. 9, 1972, pp. 646–651.

[3]DeLaurier, J. D., "Prediction of Tethered-Aerostat Response to Atmospheric Turbulence," *Journal of Aircraft*, Vol. 14, No. 4, 1977, pp. 407–409.

[4]Jones, S. P., and Krausman, J. A., "Nonlinear Dynamic Simulation of a Tethered Aerostat," *Journal of Aircraft*, Vol. 19, No. 8, 1982, pp. 679–686.

[5]Jones, S. P., and DeLaurier, J. D., "Aerodynamic Estimation Techniques for Aerostat and Airships," *Journal of Aircraft*, Vol. 20, No. 2, 1983, pp. 120–126.

[6]Humphreys, D. E., "Validation of the Dynamic Characteristics of a Towed, Scaled Aerostat," *Proceedings from the 12th AIAA Lighter-Than-Air Systems Technology Conference*, Vol. 1, AIAA, Reston, VA, 1997, pp. 227–236.

[7]Redd, T., Bland, R., and Bennet, R. M., "Stability Analysis and Trend Study of a Balloon Tethered in a Wind, with Experimental Comparisons," NASA TN D-7272, Oct. 1973.

[8]Badesha, S., and Jones, S. P., "Aerodynamics of the TCOM 71M Aerostat," *Proceedings from the 10th AIAA Lighter-Than-Air Systems Technology Conference*, Vol. 1, AIAA, Washington, DC, 1993, pp. 36–42.

[9]Jones, S. P., and Shroeder, L. D., "Nonlinear Dynamics Simulation of a Tethered Aerostat: A Fidelity Study," *Journal of Aircraft*, Vol. 38, No. 1, 2001, pp. 64–68.

[10]Etkin, B., "Stability of a Towed Body," *Journal of Aircraft*, Vol. 35, No. 2, 1998, pp. 197–205.

[11]Nahon, M., "A Simplified Dynamics Model for Autonomous Underwater Vehicles," *Proceedings of the 1996 Inst. of Electrical and Electronics Engineers Symposium on Autonomous Underwater Vehicle Technology*, 1996, Vol. 1, IEEE, Piscataway, NJ, pp. 373–379.

[12]Jones, G. W., Jr., "Investigation of the Effects of Variations in the Reynolds Number Between 0.4×10^6 and 3.0×10^6 on the Low-Speed Aerodynamic Characteristics of Three Low-Aspect-Ratio Symmetrical Wings with Rectangular Plan Forms," *NACA* RM L52G18, Sept. 1952.

[13]McCormick, B. W., *Aerodynamics, Aeronautics and Flight Mechanics*, Wiley, New York, 1995, pp. 158–175.

[14]Newman, J. N., *Marine Hydrodynamics*, MIT Press, Cambridge, MA, 1989, p. 144.

[15]Driscoll, R., and Nahon, M., "Mathematical Modeling and Simulation of Moored Buoy System," *Proceedings of Oceans*, Vol. 1, 1996, pp. 517–523.

[16]Rao, S. S., *Mechanical Vibrations*, Addison Wesley Longman, Reading, MA, 1995, pp. 503–506.